

## Interfacial flows in corrugated microchannels: flow regimes, transitions and hysteresis

Majid Ahmadydarab<sup>a</sup>, Zhong-Sheng (Simon) Liu<sup>b</sup>, James J. Feng<sup>a,c,\*</sup>

<sup>a</sup>*Department of Chemical and Biological Engineering, University of British Columbia, Vancouver, BC V6T 1Z3, Canada*

<sup>b</sup>*NRC Institute for Fuel Cell Innovation, 4250 Wesbrook Mall, Vancouver, BC V6T 1W5, Canada*

<sup>c</sup>*Department of Mathematics, University of British Columbia, Vancouver, BC V6T 1Z2, Canada*

---

### Abstract

We report simulations of gas-liquid two-phase flows in microchannels periodically patterned with grooves and ridges. A constant effective body force is applied on both fluids to simulate a pressure-driven creeping flow, and a diffuse-interface model is used to compute the interfacial evolution and the contact line motion. Depending on the body force, capillary force and the level of liquid saturation, a number of flow regimes may appear in the corrugated microchannel: gas flow, blockage, liquid flow, bubble-slug flow, droplet flow, annular flow and annular-droplet flow. A map of flow regimes is constructed for a set of geometric and flow parameters starting from a prescribed initial configuration. Some of the regimes are new, while others have been observed before in straight tubes and pipes. The latter are compared with previous experiments in terms of the regime map and the holdup ratio. The transition among flow regimes shows significant hysteresis, largely owing to the pinning of the interface at sharp corners in the flow conduit. Hysteresis is reduced if the sharp corners are rounded. Under the same operating conditions, different flow regimes can be realized from different initial conditions. The roles of geometry and wettability of the channel walls are also elucidated.

*Keywords:* Gas-liquid two-phase flow, moving contact line, Cahn-Hilliard

---

\*Corresponding author

*Email address:* jfeng@chbe.ubc.ca (James J. Feng)

## 1. Introduction

Traditionally, interfacial flows in pores of microscopic dimensions are studied in the context of displacing oil by water in enhanced oil recovery (Marle, 1981; Lenormand et al., 1988). More recently, such flows have taken on new significance in applications such as microfluidics (Joanicot and Ajdari, 2005; Atencia and Beebe, 2005; de Loos et al., 2010) and proton-exchange membrane (PEM) fuel cells (Soares et al., 2005; Zhang et al., 2006; Nam et al., 2009). The small spatial dimensions have several implications. For one, gravity and inertia are often negligible since the Bond number and Reynolds number are much below unity. Meanwhile, capillarity plays a much more important role. This is manifested not only by a curvature-related pressure difference between the two phases, but also by detailed features of the interfacial dynamics, including interfacial deformation and rupture and the motion of three-phase contact lines on the solid wall.

The prevailing theoretical treatment is a lumped-parameter approach. A common basis for most models is an “extended Darcy’s law”, with the capillary pressure either taken as the driving force for the flow or as a resistance to be overcome in capillary breakthrough (Wang, 2004; Djilali, 2007). This is then supplemented by two empirical correlations: an effective permeability expressed in terms of the saturation and the Leverett J-function relating the capillary pressure to the saturation (Kumbur et al., 2007). The main shortcoming of this approach is its empiricism; it is not based on hydrodynamic principles and concrete flow mechanisms. In fact, conflicting assumptions have been made in the literature regarding the driving force of the flow (Wang, 2004; Litster et al., 2006), to produce contradictory predictions. Because of the small dimensions and complex flow geometry, direct observation of the interfacial dynamics is difficult. Thus there is little solid experimental data to guide the modeling efforts.

Hence comes the motivation for the present study. By accurate numerical simulation, we elucidate the detailed fluid dynamics on the pore length scale. The flow geometry consists in an axisymmetric tube with periodic expansion and contraction. These simulate the pore chambers and throats in typical porous medium (Cerepi et al., 2002). An axial pressure gradient is applied to drive a gas and a liquid down the conduit. The focus will be on the interfacial morphology under different flow conditions, which will be categorized in

terms of flow regimes. In this connection, we briefly review the flow regimes known in gas-liquid flows in smooth tubes and pipes.

The gas-liquid flow regimes have been summarized into maps in terms of the superficial gas and liquid velocities (Mandhane et al., 1974; Taitel and Dukler, 1976; Taitel et al., 1980; Barnea et al., 1980). In *macroscopic* pipes and tubes, on the order of 1 cm in diameter, three categories of flow regimes have been reported: separated (e.g., annular and stratified flows), intermittent (e.g., slug and churn flows), and distributed (e.g., bubbly and droplet flows). *Microchannels*, with a diameter on the order of 1 mm or less, have received much attention recently (Hassan et al., 2005). The shrinking length scale causes some subtle changes in the flow regimes. For example, in horizontal microchannels, the stratified regime is never seen because the importance of gravity is much reduced by the small dimensions (Damianides and Westwater, 1988; Fukano and Kariyasaki, 1993). Mishima et al. (1993) also reported suppression of the churn flow regime in small channels. This probably reflects the declining role of inertia, as churn flows prevail for the highest flow rates for both the gas and the liquid. Aside from these, the familiar bubbly, slug, churn and annular flow regimes are seen, and the regime map is qualitatively the same as in larger tubes (Hassan et al., 2005; de Loos et al., 2010).

Our work differs from the above in several aspects. First and foremost, we strive for a fully-resolved hydrodynamic computation of the fluid dynamics and interfacial evolution on the scale of the pores. The aim is to establish an understanding of the mechanisms producing the flow regimes from first principles. This contrasts with the existing literature that relies almost exclusively on experimental observations. Second, we adopt a geometric and mechanical setup of the problem relevant to water transport in the gas-diffusion medium of PEM fuel cells (Djilali, 2007; Nam and Kaviani, 2003), which differs from previous studies. For one, we adopt a periodically corrugated axisymmetric flow conduit to simulate the geometry of complex pores with pore chambers and pore throats. In addition, we consider pore sizes on the order of 10 microns (Schulz et al., 2007), much smaller than the tubes and pipes of existing studies. As a result, interfacial tension is expected to dominate gravity and inertia. Moreover, the flow is driven by an external pressure gradient applied to both components. This way, the gas and liquid flow rates are not control parameters but outcomes of the fluid dynamics. Finally, we give special attention to the wetting properties of the solid walls. In gas-diffusion medium, hydrophobic coating is frequently applied to facili-

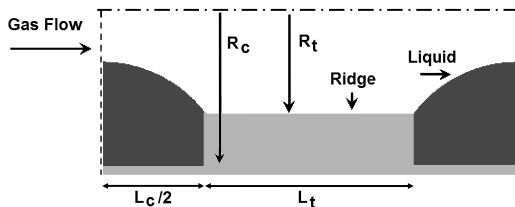


Figure 1: Schematics of the periodic flow geometry. The top of the domain is the axis of symmetry, and periodic boundary conditions are imposed between the left and right sides. Initially the liquid rests in the groove representing a pore chamber.

tate water removal (Kumbur et al., 2007). In the two-phase flow literature, a few authors have experimented with modifying the wettability of the smooth surface of tubes (Barajas and Panton, 1993; Cubaud et al., 2006).

The main results of the present study are the following. We have constructed a flow regime map for gas-liquid flows in the corrugated channel geometry. Interestingly, we have detected significant hysteresis in the transitions among flow regimes, and different flow regimes can be realized under identical conditions if starting from different initial morphologies. The regimes are understood as outcomes of the interfacial dynamics, including pinning of the contact line at sharp corners, wetting and dewetting on solid surfaces, and rupture and coalescence of the interface. Where comparable, the flow regimes are in remarkable agreement with previous experiments.

## 2. Problem setup and methodology

Consider an axisymmetric corrugated microchannel that is periodically patterned with grooves and ridges (Fig. 1). The motivation for having the corrugation is to model the contraction and expansion in micropores contained in a porous medium. Therefore, the narrow part of the flow conduit over the ridge represents the pore throat with radius  $R_t$  and length  $L_t$ , and the wide part in the groove the pore chamber with radius  $R_c$  and length  $L_c$ . From these, we define three length ratios  $\alpha = L_c/L_t$ ,  $\beta = R_c/R_t$  and  $\gamma = L_t/R_t$ .

The prominent features of the fluid dynamic problem include the deformation and movement of the interface, the three-phase contact line, and the surface wettability. These will be handled in a diffuse-interface framework using the Cahn-Hilliard model (Jacqmin, 2000; Yue et al., 2006; Zhou et al.,

2010). A phase-field variable  $\phi$  is introduced as the order parameter for the gas-liquid system, such that  $\phi = 1$  in the liquid and  $\phi = -1$  in the gas. The position of the interface is given by  $\phi = 0$ , with  $\phi$  varying steeply but continuously across the interface. The advection and diffusion of  $\phi$  are governed by the Cahn-Hilliard equation

$$\frac{\partial \phi}{\partial t} + \mathbf{u} \cdot \nabla \phi = M \nabla^2 G, \quad (1)$$

where  $M$  is the mobility constant for Cahn-Hilliard diffusion,  $\mathbf{u}$  is the velocity vector and the chemical potential  $G = \lambda[-\nabla^2 \phi + (\phi^2 - 1)\phi/\epsilon^2]$  arises from the variation of the system free energy with respect to  $\phi$  (Yue et al., 2004; Feng et al., 2005). In this expression,  $\lambda$  is the mixing energy density and  $\epsilon$  is the capillary width representative of the interfacial thickness. In equilibrium,  $\lambda$  and  $\epsilon$  are related to the surface tension  $\sigma$ :

$$\sigma = \frac{2\sqrt{2}}{3} \frac{\lambda}{\epsilon}. \quad (2)$$

For the flow in microscopic pores of interest here, estimation from typical pore sizes and operating conditions in the gas diffusion medium gives Reynolds and Bond numbers on the order of  $10^{-2}$  (Zhang et al., 2006; Koido et al., 2008). Thus, we neglect gravity and inertia and focus on creeping flows in which capillary forces play an important role. Now one can write out the continuity and momentum equations for the two-phase system in a unified form as follows:

$$\nabla \cdot \mathbf{u} = 0, \quad (3)$$

$$\nabla p = \nabla \cdot [\mu(\nabla \mathbf{u} + \nabla \mathbf{u}^T)] + G \nabla \phi, \quad (4)$$

in which  $G \nabla \phi$  is the diffuse-interface representation of the interfacial tension, and

$$\mu = \frac{1 + \phi}{2} \mu_l + \frac{1 - \phi}{2} \mu_g \quad (5)$$

is the effective viscosity that varies across the interface between those of the liquid  $\mu_l$  and gas  $\mu_g$ . Now the gas-liquid interface is no longer a *boundary* that requires boundary conditions. Equations (3) and (4) are solved together with the Cahn-Hilliard equation (1).

We will consider flow through the periodic geometry of Fig. 1 driven by a constant pressure gradient. It is convenient to replace the prescribed

pressure drop over one period of the channel by a constant body force  $\mathbf{B}$  acting on both components along the flow direction such that the pressure will be periodic as well as the velocity field. Thus, Eq. (4) will be modified as

$$\nabla p = \nabla \cdot [\mu(\nabla \mathbf{u} + \nabla \mathbf{u}^T)] + G\nabla\phi + \mathbf{B}, \quad (6)$$

and the magnitude of the effective body force  $B$  will be a key control parameter for the flow problem.

The initial condition typically has the liquid and gas at rest in the domain, with a certain initial configuration for the gas-liquid interface. For example, the liquid may initially occupy the pore chamber as shown in Fig. 1. This initial configuration specifies the liquid saturation  $S$  in the pore, defined as the volume fraction of the liquid relative to the entire pore volume. The saturation  $S$  is an important control parameter of the problem, and remains constant for the duration of each flow simulation. Under the constant driving force  $B$ , both components start to flow and eventually a steady, time-periodic or quasi-periodic flow pattern establishes itself.

Periodicity is imposed on  $\mathbf{u}$ ,  $p$  and  $\phi$  between the left and right boundaries of the axisymmetric computational domain depicted in Fig. 1. The top of the domain is the axis of symmetry on which we impose symmetry conditions  $\partial/\partial r = 0$  and  $u_r = 0$ . On the solid substrate, the following conditions are used:

$$\mathbf{u} = 0, \quad (7)$$

$$\mathbf{n} \cdot \nabla G = 0, \quad (8)$$

$$\lambda \mathbf{n} \cdot \nabla \phi + f'_w(\phi) = 0, \quad (9)$$

where  $\mathbf{n}$  is the unit normal vector pointing from the fluid into the wall. Of these, the first condition asserts zero slip and that the contact line motion is solely due to Cahn-Hilliard diffusion. The second denotes zero flux through the walls. The third is the diffuse-interface specification of the wetting angle. It is the natural boundary condition arising from the variation of the wall energy  $f_w$ :

$$f_w(\phi) = -\sigma \cos \theta_s \frac{\phi(3 - \phi^2)}{4} + \frac{\sigma_{ls} + \sigma_{gs}}{2}, \quad (10)$$

which is the interfacial energy between the fluids and the solid substrate (Jacqmin, 2000; Yue et al., 2010). In the fluid bulk phases,  $f_w$  recovers  $\sigma_{ls}$  and  $\sigma_{gs}$ , the liquid-solid and gas-solid interfacial tensions, which determine

the static contact angle  $\theta_s$  via Young’s equation  $\sigma \cos \theta_s = \sigma_{gs} - \sigma_{ls}$ . Equation (9) implies an equilibrium between the fluid components and the wall, such that the dynamic contact angle  $\theta_d$  remains at the static value  $\theta_s$  up to the leading order. By replacing the natural boundary condition of Eq. (9) by a dynamic equation specifying how fast the interfacial profile equilibrates on the solid substrate, one may introduce a  $\theta_d$  that increases when advancing and decreases when receding (Yue et al., 2010; Yue and Feng, 2011b). For the purpose of the present study, we need a simple contact-line model with a minimum of model parameters. Thus, we have left out the dependence of the dynamic contact angle on flow.

The most important dimensionless control parameter is  $F = BL^2/\sigma$ , where the characteristic length  $L$  is chosen to be the throat radius ( $R_t$ ). This can be seen as an effective Bond number as  $B$  is an effective body force. Alternatively, if one thinks of the pressure gradient as producing a characteristic speed for the viscous flow in the channel,  $F$  may be viewed as a capillary number. Two other dimensionless parameters are the liquid saturation  $S$  and liquid-gas viscosity ratio  $k = \mu_l/\mu_g$ . In addition, the diffuse-interface model introduces two “mesoscopic” parameters, the Cahn number  $Cn = \epsilon/L$  and the parameter  $\Lambda = l_d/L$ . The former is the ratio between the interfacial thickness and the macroscopic length, while the latter between the diffusion length  $l_d = (\mu_l\mu_g)^{1/4}M^{1/2}$  and  $L$  (Yue et al., 2010; Yue and Feng, 2011b). These must be chosen judiciously based on the following considerations.

For diffuse-interface methods to produce accurate results, one must attain both “model convergence” and “mesh convergence” (Yue et al., 2006; Zhou et al., 2010). The former requires that the interface be thin enough to approximate the sharp-interface limit, and the latter that the thin interface be resolved by a sufficient number of grid points. In previous publications, we have validated the algorithm against sharp-interface computations, and suggested guidelines in choosing  $\epsilon$  and  $Cn$  (Yue et al., 2004, 2006; Zhou et al., 2010). For the current geometry, numerical experimentation has confirmed these guidelines.

The diffuse-interface model regularizes the contact-line singularity by Cahn-Hilliard diffusion, and the mobility  $M$  largely determines the velocity of the contact line. There are several interesting questions about this approach, which have been investigated at length in separate studies (Yue et al., 2010; Zhou et al., 2010; Yue and Feng, 2011a,b). For our purpose here, we only note that the diffusion length  $l_d$  is a counterpart of the slip length commonly used in sharp-interface models (Yue et al., 2010). In the

simulations presented here, we have used  $Cn = 0.01$  and  $\Lambda = 0.01$ , which according to our previous studies are sufficient for the sharp-interface limit (Gao and Feng, 2009; Yue et al., 2010).

We solve the governing equations with the boundary conditions using an in-house finite-element package AMPHI (Yue et al., 2006; Zhou et al., 2010). It employs unstructured triangular elements that are adaptively refined and coarsened as the interface moves. An implicit time-marching scheme is used, with Newton iterations at each time step. Yue et al. (2006) and Zhou et al. (2010) have presented detailed descriptions of the numerical method and performed extensive validations. In the problems simulated here, we have done mesh-refinement tests as well to ensure that the numerical results have converged with the grid size. In particular, the interfacial curvature is accurately computed so that no parasitic flow is detectable. For the results to be presented, the fine grid size at the interface is  $\epsilon/2$ , and the bulk grid size is around  $5\epsilon$ .

### 3. Results

A large number of flow regimes have been observed in our simulations, and hysteresis is a prominent feature in the transition between regimes. Related to hysteresis is the observation that under identical material, geometric and operating conditions, different regimes can be reached starting from different initial conditions.

To present this rather complex picture in a systematic way, we will first describe all the observed regimes reached from a certain initial condition at different operating parameters  $S$  and  $F$ . A flow regime map can thus be constructed in the  $(F, S)$  plane. Next, we will discuss hysteresis in the sense of dependence on the flow history, with  $F$  being decreased or increased gradually for a fixed  $S$ , and on the initial condition. This history dependence turns out to be closely related to our corrugated geometry, and we will explore the effect of replacing the sharp corners by rounded ones. Finally, we examine the role of solid wettability on the flow pattern.

#### 3.1. Flow regimes

First we construct a map of flow regimes for a “baseline” setup of the problem. We fix the geometric parameters at  $\alpha = 1$ ,  $\beta = 2$  and  $\gamma = 2$ , the wetting angle at  $\theta_s = 135^\circ$ , and the liquid-gas viscosity ratio at  $k = 18$ . The geometric parameters are chosen with a view of actual pore geometries (e.g.,

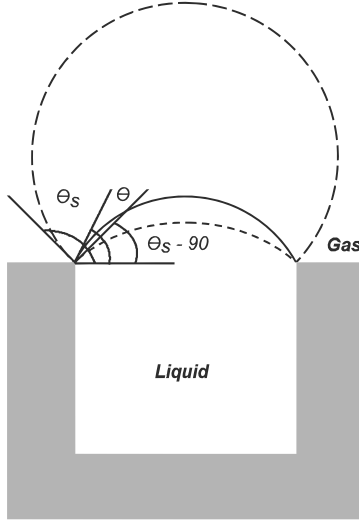


Figure 2: Schematic illustration of the condition for contact line pinning. The solid curve is the gas-liquid interface, and the dashed curves indicate its limiting positions before the contact line depins from the corner.

Cerepi et al., 2002). We have varied them within a modest range, but will not present the results below as they add little new physics. The  $\theta_s$  and  $k$  values correspond to typical operating conditions in the gas-diffuse medium of PEM fuel cells, with water and air at 80°C. Initially the liquid sits entirely in the pore chambers, as depicted in Fig. 1. The maximum realizable liquid saturation is then constrained by the depinning of a contact line at the sharp corner, or by the liquid meniscus reaching the axis of symmetry and thus forming a liquid bridge. As illustrated in Fig. 2, the Gibbs criterion for pinning at the 90° corner requires (e.g., Oliver et al., 1977):

$$\theta_s - 90^\circ < \theta < \theta_s. \quad (11)$$

With the large contact angle  $\theta_s = 135^\circ$  in our case, the maximum saturation is  $S = 0.78$  corresponding to the geometric condition of the liquid arc reaching the top of the computational domain. With less liquid, the interface lowers and may depin from the corner. So the minimum  $S$  is zero. At each prescribed  $S$ , the interface initially assumes a shape of a circular arc. Then a constant body force  $F$  is applied to initiate the flow, which evolves into a well-established pattern that is recorded as a regime.

For the baseline setup of the problem, all the flow regimes observed are depicted in Fig. 3 in the  $F$ - $S$  parameter space. For the lowest values of

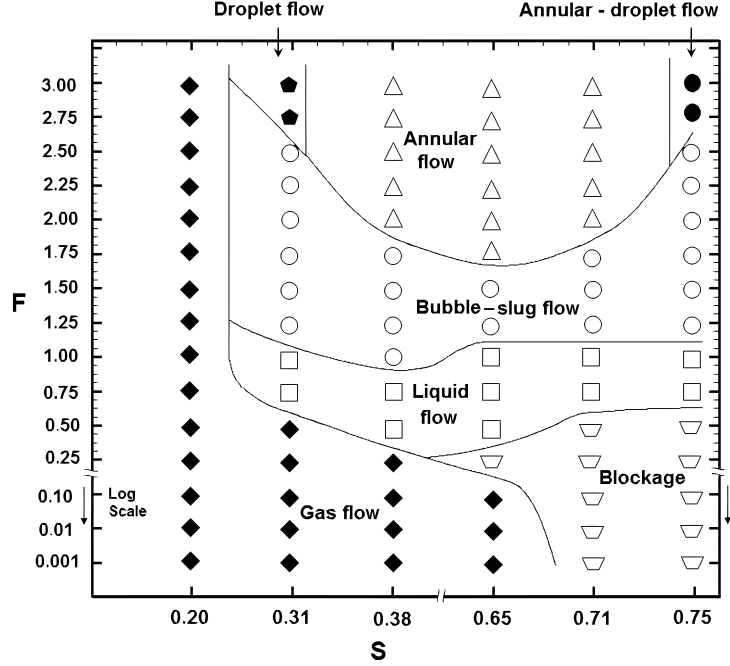


Figure 3: Flow regime map for the baseline model. Note that the columns of symbols are spaced for clarity and not according to the exact  $S$  values.

the driving force  $F$ , one of two states prevails depending on the level of saturation. For low  $S$ , the liquid mostly stays within the pore chamber or groove of the channel. The gas flow in the middle is not strong enough to drive the liquid into the pore throat. This is the regime of *gas flow*, shown in Fig. 4. Pinning of the interface at the downstream corner of the pore chamber prevents the liquid from wetting the pore throat. For higher saturation, even the gentle driving force is able to cause the liquid meniscus to raise a crest, which merges in the center of the conduit to form a liquid bridge that completely blocks the gas flow. This *blockage regime* is depicted in Fig. 5. Though not obvious in the plot, the liquid bridge is slightly asymmetric fore and aft, with differing pinning angles at the corners. The net force due to interfacial tension balances the driving force  $F$ .

With increasing  $F$ , two routes of evolution are possible depending on  $S$ . For the lowest saturation ( $S = 0.2$  in Fig. 3), the liquid remains in the groove even for the strongest driving force. The gas flow regime persists. For higher  $S$ , a series of flow regimes are observed with increasing  $F$ . We will illustrate

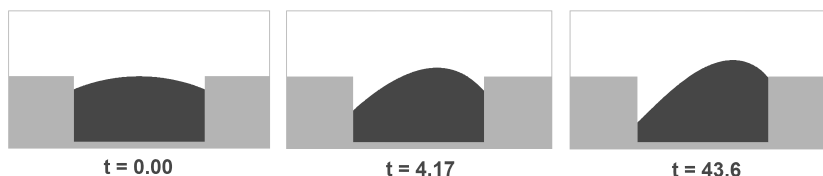


Figure 4: The gas flow regime achieved for a low saturation ( $S = 0.38$ ) under a gentle driving force  $F = 0.25$ . The meniscus is circular at the start of the simulation, with no flow ( $t = 0$ ). It deforms moderately in the steady state ( $t = 43.6$ ). The upper edge of the plots corresponds to the axis of the pore.

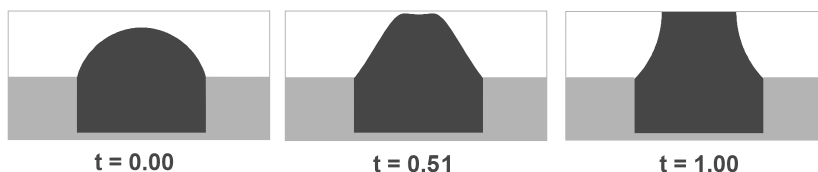


Figure 5: Development of complete blockage in the microchannel at  $F = 0.001$  and  $S = 0.75$ .



Figure 6: Development of the liquid flow regime with  $F = 0.75$  and  $S = 0.38$ . Because of the axisymmetry of the geometry, as the liquid moves from the chamber into the pore throat, its projected area on the meridian plane being plotted increases even though its volume is conserved.

them by using  $S = 0.38$ .

The first transition gives rise to the *liquid flow regime* depicted in Fig. 6. The liquid is drawn from the pore chamber into the throat and forms a liquid bridge spanning the cross section much like in the the blockage regime. But now the greater  $F$  deforms it and moves it downstream until it merges with the liquid bridge of the next period. This produces a continuous liquid stream in the middle of the pore, with a gas pocket trapped in the chamber. At higher  $S$ , the blockage regime of Fig. 5 gives way to the liquid flow regime via a similar process.

A still higher  $F$  produces the *bubble-slug flow* regime (Fig. 7). In the



Figure 7: Development of the bubble-slug regime at  $F = 1.75$  and  $S = 0.38$ .



Figure 8: Development of the annular flow regime at  $F = 3$  and  $S = 0.38$ .

literature, *bubbles* are sometimes defined as gaseous blobs having an effective diameter below 75% of the tube diameter, and *slugs* as larger ones (de Loos et al., 2010). In our context there is no need to distinguish them. This regime resembles the liquid flow regime except for the discrete gas bubbles or slugs carried along the center of the conduit. Compared with Fig. 6, the stronger  $F$  elongates the liquid bridge axially so as to create a lamella oriented more or less along the flow direction ( $t = 12.7$ ). When the undulation of the lamella causes a secondary coalescence in the center, a gas bubble or slug is entrapped ( $t = 17$ ). The flow evolves into a time-periodic pattern with the passing of the bubble or slug through the pore. The gas pocket entrapped in the corner of the chamber maintains an essentially constant shape with recirculation inside.

If  $F$  is increased further, the *annular flow regime* prevails for most of the saturation values tested (Fig. 8). Similar to the bubble-slug regime, the liquid moves out of the pore chamber into the pore throat. The fast gas flow spreads the liquid lamella downstream, keeping it close to the solid ridge and preventing the formation of a liquid bridge. When the lamella connects with the remaining liquid in the chamber ( $t = 10.9$ ), a continuous liquid annulus is formed that encloses the gas flow in the core. Two variations of this are the *droplet flow* and *annular-droplet flow* regimes, which appear respectively for very low and very high saturations. At low  $S$ , there is not enough liquid to form a continuous annulus. Instead, some of the liquid is torn off by the gas stream to form droplets (Fig. 9a). At higher  $S$ , the abundance of liquid is such that both the annulus and droplets are created (Fig. 9b).



Figure 9: Variants of the annular flow regime: (a) droplet flow at  $F = 3$  and  $S = 0.31$ ; (b) annular-droplet flow at  $F = 3$  and  $S = 0.75$ . Both are time-periodic configurations, and the liquid film on the ridge in (a) has stopped moving downstream.

### 3.2. Hysteresis and dependence on initial configuration

In constructing the map of flow regimes in Fig. 3, we have always started from the initial condition depicted in Fig. 1, with a prescribed amount of liquid sitting in the pore chamber. With zero initial velocity, a prescribed body force is suddenly applied to both components, and the flow evolves till a robust pattern emerges, which may be steady or time-periodic.

By *hysteresis*, we refer to how the flow regime realized depends on the history of varying the control parameters. If we start inside a certain regime, say annular flow, and decrease  $F$  in small steps, will we reach the bubble-slug flow and the other regimes successively that lie below in the map? What if we start from the gas flow regime at a small  $F$ , and then gradually increase  $F$ ? Will the boundary between regimes shift depending on whether a parameter is increased or decreased? If we start from different initial states, and suddenly impose the same control parameters, will we arrive at different final states?

To probe these questions, we have tested two saturation values,  $S = 0.31$  and  $S = 0.71$ . In each case, we ramp up the flow by increasing  $F$  gradually starting from an initial condition in the gas flow or blockage regimes. This is called the forward path. We then ramp down the flow, starting with the end state of the forward path, by decreasing  $F$  gradually. This will be the backward path. Figure 10 compares the forward and backward paths with the regimes realized from the baseline model (i.e., starting from the standard initial condition of Fig. 1) taken from the regime map of Fig. 3. While the baseline model predicts multiple regimes, the forward path encounters only one transition: from gas flow (for  $S = 0.31$ ) or blockage (for  $S = 0.71$ ) to the liquid flow regime. Then liquid flow persists, not only till the highest  $F$  on

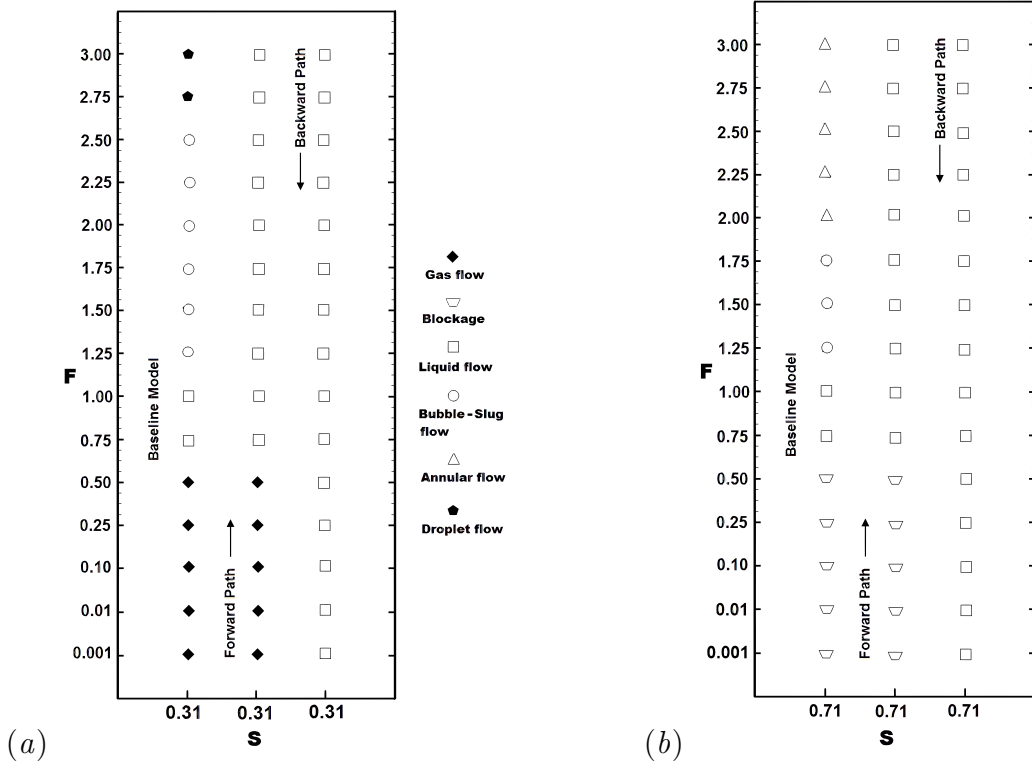


Figure 10: Hysteresis or path dependence of the flow regimes at saturation  $S = 0.31$  (a) and  $S = 0.71$  (b). Other parameters are the same as have produced the flow regime map in Fig. 3.

the forward path, but also on the entire backward path, down to  $F$  as small as  $10^{-3}$ . Therefore, the flow regimes show an exceedingly strong dependence on the history of changing  $F$ , so much so that the term “hysteresis” becomes somewhat inappropriate as it typically refers to the delay of a transition, not its utter absence.

The dominance of the liquid flow regime can be rationalized from the interfacial morphology. Once the pore throat is completely filled with liquid and the gas is sealed within the pore chamber (last frame of Fig. 6), the throughput of the pore is entirely liquid. Varying the driving force  $F$  mostly changes the liquid flow rate, with a minor effect on the shape of the interface and the recirculation within the gas. In particular, the interface is pinned at the upstream corner, and there is no mechanism to liberate the gas from the

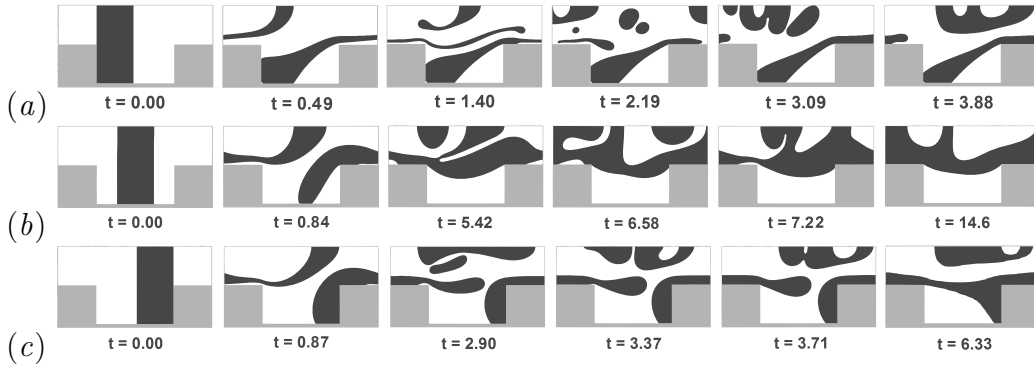


Figure 11: Dependence of flow regimes on the initial configuration. (a) Droplet flow develops from a liquid bridge initially wetting the upstream wall of the pore chamber. (b) Bubble-slug flow develops from a liquid bridge initially in the middle of the pore chamber. (c) Annular-droplet flow develops from a liquid bridge initially attached to the downstream wall of the pore chamber.  $F = 3$ ,  $S = 0.38$ , and the other conditions are the same as in the baseline model.

confinement of the pore chamber. Therefore transition to other flow regimes is not possible. This contrasts with the setup of the baseline model, with gas initially in the central region of the pore.

To further demonstrate the effect of the initial configuration on the final flow regimes, we start with a liquid bridge spanning the entire cross section of the pore chamber at different axial positions (first frames of Fig. 11*a,b,c*), all having the same saturation  $S = 0.38$ . When the same body force  $F = 3$  is imposed, the flow evolves into three different regimes: droplet, bubble-slug and annular-droplet flows. None is identical to the annular flow regime obtained from the baseline setup (Fig. 8).

In these particular cases, the final outcome depends on whether the initial liquid bridge adheres to parts of the chamber walls. In Fig. 11(*a*), a liquid sheet remains attached to the upstream corner of the pore chamber and coats the pore throat as well. Figure 11(*c*) is similar but has the liquid sheet attached to the downstream side of the chamber. In Fig. 11(*b*), the liquid bridge never wets these parts of the chamber; it is readily stretched into the throat and eventually detaches entirely from the base of the chamber. Although these details are specific to the initial morphologies tested, their implication is general: initial morphology can affect the flow regimes achieved under identical operating conditions. We have tested other initial conditions at different operating conditions with the same upshot. For brevity we will

not show the detailed results.

In the simulations presented here, hysteresis stems from the fact that interfacial tension and contact-line pinning at corners set up energy barriers between possible interfacial morphologies. A transformation would require high-cost interfacial elongation and contact-line depinning. Thus, the interfacial morphology can be remarkably stable and insensitive to changes in operating conditions. An overarching observation is that the hysteresis and missing flow regimes owe much to the corrugated geometry in our microchannel. This explains why prior studies in smooth tubes and pipes of various sizes have not reported hysteresis (Taitel and Dukler, 1976).

### 3.3. Geometric effect: rounded corners

Given the prominent role of the corrugated geometry in determining the flow regimes and transitions, a natural question is what if we remove the sharp corners and make the constriction gradual and smooth. This has been tested by replacing the solid ridge in the baseline model, with  $\alpha = 1$ ,  $\beta = 2$  and  $\gamma = 2$ , by a rounded semi-circle. All other conditions are the same as the baseline model with sharp corners. Note that our mesh generator approximates curved boundaries by short line segments. Numerical experimentation has shown that with sufficiently fine division, this presents no spurious effects.

Starting from the same initial morphology with liquid resting in the pore chamber, imposing different  $F$  values leads to different regimes in the rounded-corner geometry. These regimes are compared in Fig. 12 with those in the sharp-corner geometry for a fixed  $S = 0.38$ . Whereas gas flow gives rise to liquid flow when  $F$  exceeds 0.5 with sharp corners, the rounded geometry produces a core-annular morphology with a liquid core enclosed in a gas shell, called the *shell flow regime* (Fig. 13). Absent the sharp corner to pin the interface and anchor the liquid onto the ridge, as shown previously in Fig. 6, the liquid eventually detaches from the solid protrusion, which is hydrophobic with  $\theta_s = 135^\circ$ . Thus a gas shell is formed that entirely insulates the liquid from the solid walls. This is reminiscent of the lubrication scenario in oil-water core-annular flows (Joseph and Renardy, 1993) and apparent slip on textured substrates (Gao and Feng, 2009).

As  $F$  increases to 1, the shell flow gives way to a droplet flow regime (Fig. 14). In the pore with sharp corners, a similar droplet regime (Fig. 9a) occurs at the highest  $F$  for relatively low  $S$ , above the bubble-slug regime (see Fig. 3). With the rounded corners and absent corner-pinning, on the other hand, the liquid detaches from the hydrophobic solid readily at relatively low

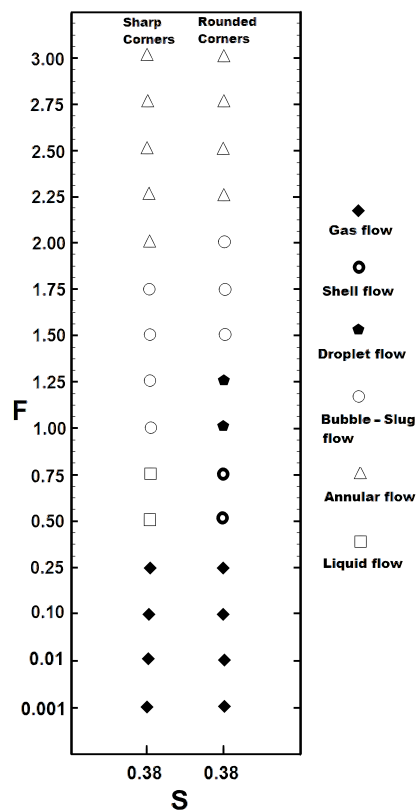


Figure 12: Flow regimes in the baseline model with rounded corners, compared with those taken from the flow map of Fig. 3 with sharp corners.  $S = 0.38$  and all other conditions are the same as in Fig. 3.

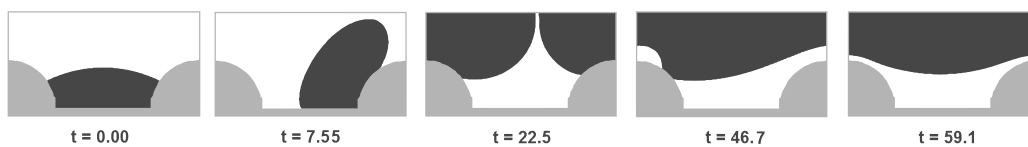


Figure 13: Development of the shell flow regime with rounded corners at  $F = 0.5$  and  $S = 0.38$ .

flow rates. The detachment is complete in the sense that no residue film is left on the solid. As  $F$  increases further, the bubble-slug and annular flow regimes appear in succession. These are similar to those observed in the sharp-cornered pores.



Figure 14: Development of the droplet flow regime with rounded corners at  $F = 1$  and  $S = 0.38$ .

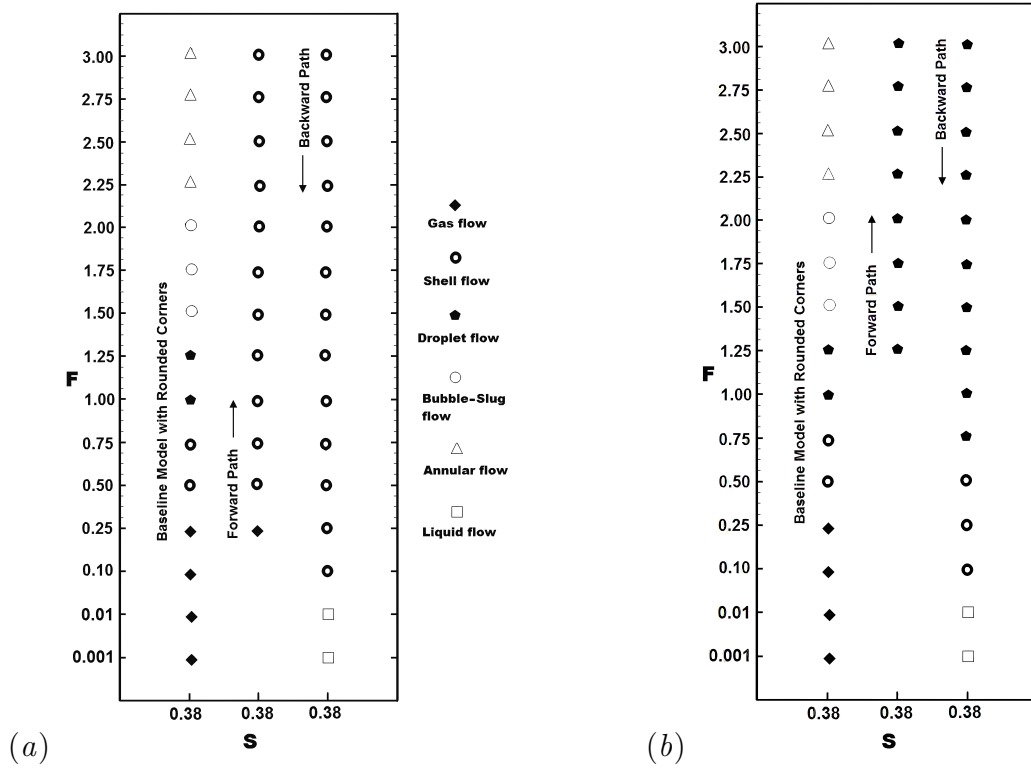


Figure 15: Hysteresis in micropores with rounded corners. At  $S = 0.38$ , forward and backward paths are traced by increasing  $F$  gradually and then decreasing it, starting from (a) the gas flow regime and (b) the droplet flow regime. The regimes achieved from the baseline model with rounded corners (Fig. 12) are shown for comparison. Other parameters are the same as in the baseline model.

To probe hysteresis in the geometry with rounded corners, we again follow a forward path by increasing  $F$  gradually, waiting for the flow regime to

develop fully at each increment, and then a backward path by decreasing  $F$  gradually. Figure 15 compares the flow regimes encountered thus with those predicted by the baseline model with the fixed initial configuration. Starting from the gas flow regime (Fig. 15a), we have a transition to the shell flow regime at  $F = 0.5$ , as in the baseline model. However, no other transitions exist on the forward path. On the backward path, the shell flow regime persists until  $F = 0.1$ , below which it gives way to liquid flow. This picture resembles Fig. 10(a), with two differences. First, the liquid flow regime is replaced by the shell flow regime. Second, there is an additional transition on the backward path, to the liquid flow regime. When starting from the droplet regime at  $F = 1.25$  (Fig. 15b), no transition takes place on the forward path. On the backward path, the droplet regime persists down to  $F = 0.75$  before turning into shell flow, which in turn transforms to liquid flow below  $F = 0.1$ . This last transition is the same as in Fig. 15(a).

To summarize the hysteresis in geometry with rounded corners, we see more transitions on the downward path than with sharp corners. In this sense, the dependence on history is lessened in comparison with the sharp-corner geometry. Without interface pinning on sharp corners, liquid flow is no longer the dominant regime. In its stead, shell flow or droplet flow becomes more prominent. In all cases, the dominance of a flow regime is thanks to the fact that once it is formed, further variation of  $F$  tends only to vary the liquid and gas flow rate, with little effect on the interfacial morphology.

### 3.4. Wettability of the solid

The tendency for the liquid or gas to adhere to the solid wall is fundamentally important to the flow situations being studied. The wetting angle reflects the energetic cost of detaching each fluid component from the solid substrate, and directly affects the shape of the interface and more subtly the motion of the contact lines (Yue et al., 2010; Yue and Feng, 2011b). The corrugated pore geometry amplifies these effects, e.g., in the pinning of the interface at corners, the detaching of the liquid from the pore chamber and its reattaching to the pore throat.

The effect of wettability is highlighted in Fig. 16, where three wetting angles are compared in a pore with sharp corners. In the hydrophilic pore (a), the liquid spreads along the ridge and eventually forms a continuous film covering the solid, yielding the annular flow regime. In the neutrally wetting case (b), the spreading of the liquid film is slower. More importantly, once the liquid reaches the downstream corner of the ridge, the interface is unable

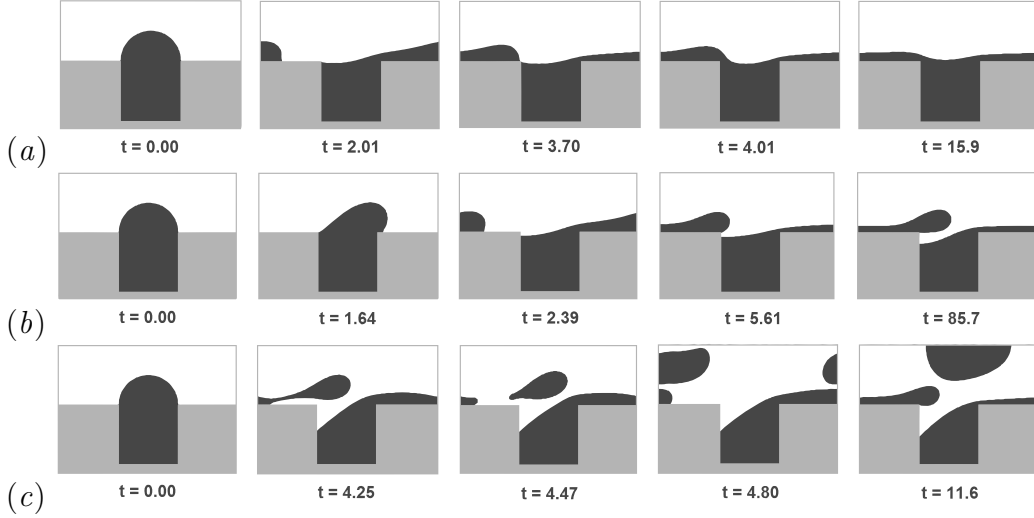


Figure 16: Effect of wall wettability on the interfacial evolution. (a) Annular flow in hydrophilic pore,  $\theta_s = 70^\circ$ ; (b) gas flow in neutrally wetting pore,  $\theta_s = 90^\circ$ ; (c) droplet flow in hydrophobic pore,  $\theta_s = 135^\circ$ . All other parameters are the same:  $F = 2$ ,  $S = 0.6$ , with geometrical parameters  $\alpha = 0.5$ ,  $\beta = 2$ ,  $\gamma = 2$ .

to depin from the corner. Thus, a liquid finger is produced at the corner that cannot merge with the liquid in the pore chamber. A gas flow regime results. Finally, in the hydrophobic pore (c), detachment of a liquid drop occurs shortly after the start of the flow, leading to the droplet flow regime. The liquid attached to the wall assumes a morphology similar to that of (b).

#### 4. Comparison with previous experiments

There exists a wealth of experimental observations on gas-liquid flows in smooth tubes and pipes, mostly of larger sizes, but more recently also of diameters below 1 mm. Before comparing our results with those, we note four important differences in the geometric and physical setup of our study.

- (a) Previous experiments control the gas and liquid flow rates and ascribe flow regimes to these rates. Our setup is such that a prescribed pressure gradient (or body force) is applied to drive both components. Therefore the gas and liquid flow rates are outcomes of the simulation rather than control parameters.

- (b) Our geometry features a pore chamber and throat, in contrast to the smooth tubes and pipes studied before. This turns out to be an important factor in determining the interfacial behavior and the flow regimes.
- (c) Previous experiments often employ high flow rates for both components, sometimes with turbulent flows. Therefore, inertia is an important factor. Our computations concern much smaller length scales and inertia is negligible. Thus the flow regimes are all for creeping flows.
- (d) Gravity is important in larger tubes, and vertical, horizontal and inclined pipes have to be studied separately. Here gravity has negligible effects, again thanks to the small length scales.

A survey of the literature shows that bubbly, intermittent, churn and annular flows are the four basic regimes in smooth straight pipes (Taitel and Dukler, 1976; Taitel et al., 1980; Hassan et al., 2005). For macroscopic horizontal pipes, a fifth regime, stratified flow, also appears.

Of these, churn flows and stratified flows are not seen in our simulations. Even in microscopic *smooth* pipes, the lack of inertial and gravitational effects is known to suppress these regimes (Fukano and Kariyasaki, 1993; Mishima et al., 1993). Therefore, their absence in our simulations is not a surprise. All the other regimes appear in our microchannel flow, albeit in somewhat modified forms. Intermittent flows consist in gas slugs or plugs moving in the middle of the pipe, being carried by the continuous liquid phase. In our simulations, we have lumped these configurations and the bubbly flows into our bubble-slug regime. The distinction between “bubbles”, “slugs” and “plug” is merely the size of the gaseous inclusion. Annular flows are also observed in our simulations, along with its variant forms of droplet and annular droplet flows.

Gas flow, liquid flow, blockage and shell flow are observed here but not in previous studies. These novel regimes are all owing to the special geometry of our microchannel. For example, if the minor phase is entirely trapped in the pore chamber, it does not contribute to the total flow rate. Thus, only one component flows, as in the gas flow or liquid flow regimes. If the driving force is weak, a liquid bridge covering the entire cross section can be anchored at the corners of the throat, thereby blocking flow of either component. These three regimes are facilitated by the pinning of the interface at sharp corners that preclude one or even both components from flowing. With rounded corners, the shell flow regime appears thanks to the lack of interface-pinning and the hydrophobicity of the solid. Although it is essentially an annular

flow with a liquid core enclosed in a gas sheath, it has never been reported previously. In a straight tube, this configuration would be unsustainable because of the Rayleigh instability.

As our control scheme prescribes  $F$  and  $S$  with the gas and liquid flow rates as outcome, it is interesting to compare quantitatively our map of flow regimes with those in the literature in terms of the superficial gas and liquid flow rates. We have attempted such a comparison for the sharp-cornered baseline model. Obviously this is feasible only for those regimes that appear in both settings, i.e., the bubble-slug and annular flow regimes. To obtain the gas and liquid flow rates  $Q_G$  and  $Q_L$ , we time-average one period of the unsteady bubble-slug regime. For steady annular flows, this is unnecessary. Defining an effective pore radius  $R_e$  based on the volume of void in each period of the pore:

$$R_e^2 = \frac{R_c^2 L_c + R_t^2 L_t}{L_c + L_t} = R_t^2 \frac{\alpha \beta^2 + 1}{\alpha + 1},$$

we can compute the superficial gas and liquid velocities using the effective cross-section area  $A_e = \pi R_e^2$ :  $V_G = Q_G/A_e$  and  $V_L = Q_L/A_e$ . Thus we may convert our dimensionless results into dimensional superficial velocities in the two flow regimes once the physical properties of the two fluids and the pore size are specified.

For an experimental benchmark, we have chosen the study of Hassan et al. (2005). These authors conducted air-water flow experiments in straight circular tubes of diameters on the order of 1 mm, and integrated their data with those in the literature to produce flow regime maps for horizontal and vertical microchannels of comparable sizes. For air and water flowing through a micropore with  $R_e = 0.5$  mm, our flow regimes are compared with the map of Hassan et al. (2005) for vertical tubes in Fig. 17. In our simulations so far, we have lumped bubbles and slugs into one regime. For the purpose of this comparison, we distinguish them by the criterion of de Loos et al. (2010); slugs are thus gas blobs longer than 75% of the effective diameter of the channel. Thus defined, our bubble-slug boundary is somewhat to the right of the experimental boundary. With  $V_G$  increasing further, the experimenters saw churn flow, which is absent in our inertialess computation. Instead we have annular flow, which occurs in the experiments further to the right. Owing to the many differences in the problem setup, the degree of similarity in Fig. 17 is intriguing. Note also that in our parameter space explored here (cf. Fig. 3), the gas velocity varies over a much wider range than the liquid

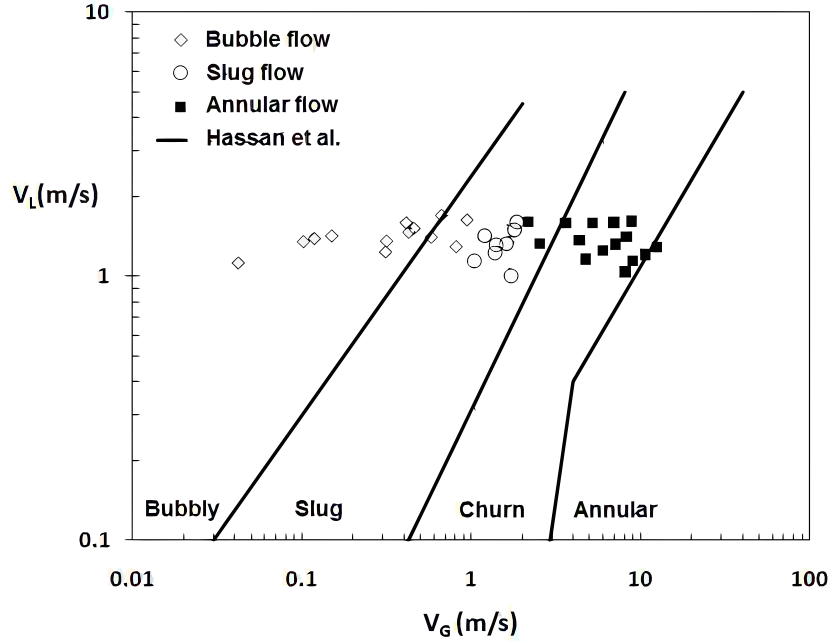


Figure 17: Flow regime map in terms of the superficial velocities: comparison of our numerical prediction with the experiment of Hassan et al. (2005). Symbols are our results and solid lines indicate regime boundaries of Hassan et al. (2005) separating the regimes indicated at the bottom.

velocity. As the same body force is applied to both phases, this discrepancy reflects the differing viscosities as well as the fact that in the two regimes plotted, the liquid stays in contact with the solid while the gas does not.

Another important parameter in two-phase flows is the *holdup ratio*  $h$ , which is defined as the ratio of superficial velocities divided by the ratio of volume fractions. The gas holdup, for example, is

$$h_G = \frac{V_G/V_L}{(1-S)/S}.$$

Obviously, when two phases are homogeneously mixed and move with the same local velocity, the superficial velocities scale with the volume fractions and  $h_G = h_L = 1$ . Thus, the holdup ratio reflects the interfacial morphology and the relative motion of the two phases. Figure 18 compares our numerical predictions of the gas holdup with the experimental data of Triplett et al.

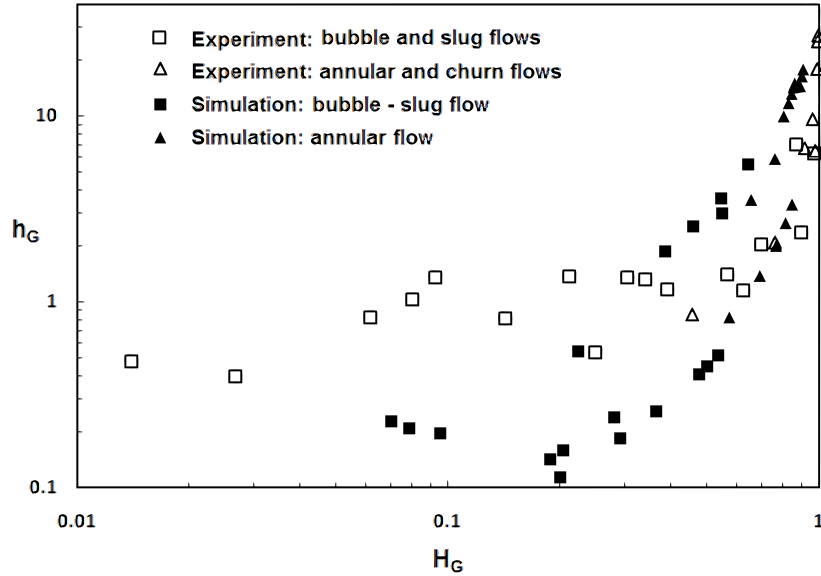


Figure 18: Gas holdup ratio as a function of the homogeneous gas fraction: comparison between our numerical prediction and the experiment of Triplett et al. (1999). The computations are for  $R_e = 0.5$  mm and the experimental data are for a circular tube of inner diameter 1.09 mm.

(1999). These authors ran air-water flows in straight circular and non-circular tubes of diameters around 1 mm, and documented the flow regimes, void fractions and frictional pressure drops. From the void fraction and superficial velocities,  $h_G$  can be obtained as a function of the homogeneous gas fraction,  $H_G = Q_G/(Q_G + Q_L)$ . Again there is remarkably close agreement between the simulation and measurement. In both cases, the gas holdup  $h_G$  tends to increase with the homogeneous gas fraction  $H_G$ , a trend well documented in the literature (Cubaud and Ho, 2004).

## 5. Conclusion

This computational study was motivated by the desire to understand the local hydrodynamics of gas-liquid flows through porous medium and microfluidic channels. To make the problem tractable, we simplified the geometry into axisymmetric tubes with periodic constrictions. Thus, we retained the features of pore chambers and pore throats, but disregarded connectivity and

branching of pores. This simplification allowed us to carry out a detailed investigation of the interfacial evolution under creeping-flow conditions. Using a diffuse-interface model, we were able to compute interfacial deformation, breakup and coalescence from hydrodynamic principles, and delineate various flow regimes based on the control parameters. Within the parameter ranges explored in this work, the main results can be summarized as follows.

- (a) Starting from an initial condition with the liquid resting inside the pore chambers, the following flow regimes may appear depending on the pressure gradient, the liquid saturation and the pore geometry: gas flow, blockage, liquid flow, shell flow, bubble-slug flow and annular flow. Annular flow has two variants: droplet flow and droplet-annular flow. These may be represented by a flow regime map on a plane extended by the liquid saturation along one axis and the nondimensionalized pressure gradient along the other.
- (b) Bubble-slug flows and annular flows are similar to those previously observed in straight tubes and pipes of macroscopic and smaller sizes. But the gas flow, blockage, liquid flow and shell flow regimes are new. Their appearance reflects to a large extent the geometric features of the flow conduit.
- (c) For bubble-slug and annular flows, the current results are compared with previous experiments. Considering the differences in geometric setup, flow-control schemes and parameter ranges, the agreement is remarkably close in terms of the boundaries between flow regimes and the holdup ratio.
- (d) The flow regimes are highly sensitive to initial conditions and flow history. Depending on whether the driving force is imposed abruptly or ramped up or down gradually, some of the flow regimes do not appear. This can be considered an extreme form of hysteresis. Different flow patterns can result from different initial conditions under identical control parameters. The dependence on flow history is largely due to interface pinning at corners, and the hysteresis effect is alleviated by rounding the sharp corners of the constriction.
- (e) Wettability of the solid surface plays an important role in shaping the final flow configuration. Generally, hydrophilicity toward the liquid encourages adherence of a liquid film along the walls, whereas hydrophobicity promotes detachment of the liquid and formation of drops in the axial region.

The significance of these results lies in that they form the basis for understanding two-phase flows in complex geometries, and contribute to a more rational treatment of such flows in applications. More specifically, we envision improving the traditional Leverett approach to porous media flows, either by basing it on a firmer theoretical basis or by replacing certain *ad hoc* elements in it. Toward this aim, ongoing work probes how the concept of relative permeability can be interpreted and calculated from hydrodynamic principles, and how the capillary pressure, based locally on pore size and curvature of the meniscus, acts to drive liquid flow or resist it until an external pressure effects a capillary breakthrough.

In view of the simplifications and limitations of the current study, we identify several outstanding issues to be tackled. First, the flow geometry needs to be represented more faithfully by accounting for branching and connection of micropores. This would call for a truly three-dimensional computation. Second, the pore size distribution must be taken into account in predicting macroscopic properties such as permeability and pressure-flow-rate relationships. Finally, it would be preferable to design a setup for the flow simulation such that the local saturation evolves as a result of the flow, as opposed to being prescribed as a control parameter. The former more closely approximates gas-liquid flows in porous media.

**Acknowledgment:** This work was supported by an NSERC Strategic Project Grant. We thank Peng Gao of the University of Science and Technology of China, G. H. (Bud) Homsy of UBC, and John Shen of Palcan Fuel Cell Co. Ltd. for helpful discussions. JJF also acknowledges partial support from the Petroleum Research Fund, the Canada Research Chair program, NSERC's Discovery Program and the Canada Foundation for Innovation.

## References

- Atencia, J., Beebe, D.J., 2005. Controlled microfluidic interfaces. *Nature* 437, 648–655.
- Barajas, A.M., Panton, R., 1993. The effects of the contact angle on two-phase flow in small diameter pipes. *Int. J. Multiphase Flow* 19, 337–346.
- Barnea, D., Shoham, O., Taitel, Y., Dukler, A.E., 1980. Flow pattern transition for gas-liquid flow in horizontal and inclined pipes: comparison of experimental data with theory. *Int. J. Multiphase Flow* 6, 217–225.

- Cerepi, A., Durand, C., Brosse, E., 2002. Pore microgeometry analysis in low-resistivity sandstone reservoirs. *J. Pet. Sci. Eng.* 35, 205–232.
- Cubaud, T., Ho, C.M., 2004. Transport of bubbles in square microchannels. *Phys. Fluids* 16, 4575–4585.
- Cubaud, T., Ulmanella, U., Ho, C.M., 2006. Two-phase flow in microchannels with surface modifications. *Fluid Dyn. Res.* 38, 772–786.
- Damianides, C.A., Westwater, J.W., 1988. Two-phase patterns in a compact heat exchanger and in small tubes, in: *Proc. 2nd UK National Conference on Heat Transfer*, Institute of Mechanical Engineers, London. pp. 1257–1268.
- Djilali, N., 2007. Computational modelling of polymer electrolyte membrane (PEM) fuel cells: Challenges and opportunities. *Energy* 32, 269–280.
- Feng, J.J., Liu, C., Shen, J., Yue, P., 2005. An energetic variational formulation with phase field methods for interfacial dynamics of complex fluids: advantages and challenges, in: *Calderer, M.C.T., Terentjev, E.M. (Eds.), Modeling of Soft Matter*. Springer, New York, pp. 1–26.
- Fukano, T., Kariyasaki, A., 1993. Characteristics of gas-liquid two-phase flow in a capillary tube. *Nucl. Eng. Des.* 141, 59–68.
- Gao, P., Feng, J.J., 2009. Enhanced slip on a patterned substrate due to depinning of contact line. *Phys. Fluids* 21, 102102.
- Hassan, I., Vaillancourt, M., Pehlivan, K., 2005. Two-phase flow regime transitions in microchannels: A comprehensive experimental study. *Nanoscale Microscale Thermophys. Eng.* 9, 165–182.
- Jacqmin, D., 2000. Contact-line dynamics of a diffuse fluid interface. *J. of Fluid Mech.* 402, 57–88.
- Joanicot, M., Ajdari, A., 2005. Droplet control for microfluidics. *Science* 309, 887–888.
- Joseph, D.D., Renardy, Y.Y., 1993. *Fundamentals of Two-Fluid Dynamics. Part II: Lubricated Transport, Drops and Miscible Liquids*. Springer-Verlag, New York.

- Koido, T., Furusawa, T., Moriyama, K., 2008. An approach to modeling two-phase transport in the gas diffusion layer of a proton exchange membrane fuel cell. *J. Power Sources* 175, 127–136.
- Kumbur, E.C., Sharp, K.V., Mench, M.M., 2007. On the effectiveness of Leverett approach for describing the water transport in fuel cell diffusion media. *J. Power Sources* 168, 356–368.
- Lenormand, R., Touboul, E., Zarcone, C., 1988. Numerical models and experiments on immiscible displacements in porous media. *J. of Fluid Mech.* 189, 165–187.
- Litster, S., Sinton, D., Djilali, N., 2006. Ex situ visualization of liquid water transport in PEM fuel cell gas diffusion layers. *J. Power Sources* 154, 95–105.
- de Loos, S.R.A., J. van der Schaaf, R.M.T., Nijhuis, T.A., de Croon, M.H.J.M., Schouten, J.C., 2010. Gas-liquid dynamics at low Reynolds numbers in pillared rectangular micro channels. *Microfluid. Nanofluid.* 9, 131–144.
- Mandhane, J.M., Gregory, G.A., Aziz, K., 1974. A flow pattern map for gas liquid flow in horizontal pipes. *Int. J. Multiphase Flow* 1, 537–553.
- Marle, C., 1981. *Multiphase flow in porous media*. Editions Technip, Paris.
- Mishima, K., Hibiki, T., Nishihara, H., 1993. Some characteristics of gas-liquid flow in narrow rectangular ducts. *Int. J. Multiphase Flow* 19, 115–124.
- Nam, J.H., Kaviany, M., 2003. Effective diffusivity and water-saturation distribution in single- and two-layer PEMFC diffusion medium. *Int. J. Heat Mass Transfer* 46, 4595–4611.
- Nam, J.H., Lee, K.J., Hwang, G.S., Kim, C.J., Kaviany, M., 2009. Microporous layer for water morphology control in PEMFC. *Int. J. Heat Mass Transfer* 52, 2779–2791.
- Oliver, J.F., Huh, C., Mason, S.G., 1977. Resistance to spreading of liquids by sharp edges. *J. Colloid Interface Sci.* 59, 568–581.

- Schulz, V.P., Becker, J., Wiegmann, A., Mukherjee, P.P., Wang, C.Y., 2007. Modeling of two-phase behavior in the gas diffusion medium of PEFCs via full morphology approach. *J. Electrochem. Soc.* 154, B419–B426.
- Soares, E.J., Carvalho, M.S., Mendes, P.R.S., 2005. Liquid water removal from a polymer electrolyte fuel cell. *J. Fluids Eng.* 127, 24–31.
- Taitel, Y., Barnea, D., Dukler, A., 1980. Modeling flow pattern transitions for steady upward gas-liquid flow in vertical tubes. *AIChE J.* 26, 345–354.
- Taitel, Y., Dukler, A.E., 1976. A model for predicting flow regime transitions in horizontal and near horizontal gas-liquid flow. *AIChE J.* 22, 47–55.
- Triplett, K.A., Ghiaasiaan, S., Abdel-Khalik, S., LeMouel, A., McCord, B.N., 1999. Gas-liquid two-phase flow regimes in microchannels. Part II: void fraction and pressure drop. *Int. J. Multiphase Flow* 25, 395–410.
- Wang, C.Y., 2004. Fundamental models for fuel cell engineering. *Chem. Rev.* 104, 4727–4766.
- Yue, P., Feng, J.J., 2011a. Can diffuse-interface models quantitatively describe moving contact lines? *Eur. Phys. J. Spec. Top.* 197, 37–46.
- Yue, P., Feng, J.J., 2011b. Wall energy relaxation in the Cahn-Hilliard model for moving contact lines. *Phys. Fluids* 23, 012106.
- Yue, P., Feng, J.J., Liu, C., Shen, J., 2004. A diffuse-interface method for simulating two-phase flows of complex fluids. *J. Fluid Mech.* 515, 293–317.
- Yue, P., Zhou, C., Feng, J.J., 2010. Sharp-interface limit of the Cahn-Hilliard model for moving contact lines. *J. Fluid Mech.* 645, 279–294.
- Yue, P., Zhou, C., Feng, J.J., Ollivier-Gooch, C.F., Hu, H.H., 2006. Phase-field simulation of interfacial dynamics in viscoelastic fluids using finite elements with adaptive meshing. *J. Comput. Phys.* 219, 47–67.
- Zhang, F.Y., Yang, X.G., Wang, C.Y., 2006. Liquid water removal from a polymer electrolyte fuel cell. *J. Electrochem. Soc.* 153, A225–A232.
- Zhou, C., Yue, P., Feng, J.J., Ollivier-Gooch, C.F., Hu, H.H., 2010. 3D phase-field simulations of interfacial dynamics in Newtonian and viscoelastic fluids. *J. Comput. Phys.* 229, 498–511.